# Fretting wear-induced sudden loss of corrosion resistance in a corrosion-resistant Ni-based alloy

Zhao Shen[1,2,3], Xiaoqin Zeng[1*], You Wang[4], Ping Lai[5], Xianglong Guo[5*], Jianqiang Zhang[6], Sergio Lozano-Perez[3], Mingxin Huang[2*]

[1] National Engineering Research Center of Light Alloy Net Forming and State Key Laboratory of Metal Matrix Composites, School of Materials Science and Engineering, Shanghai Jiao Tong University, No. 800 Dongchuan Road, Shanghai 200240, China

[2] Department of Mechanical Engineering, The University of Hong Kong, Pokfulam Road, Hong Kong, China

[3] Department of Materials, University of Oxford, Parks Road, OX1 3PH Oxford, UK

[4] School of Materials and Science, University of Science and Technology Beijing, No. 30 Xueyuan Road, Beijing 100083, China

[5] School of Nuclear Science and Engineering, Shanghai Jiao Tong University, No. 800 Dongchuan Road, Shanghai 200240, China

[6] School of Materials Science and Engineering, University of New South Wales, Sydney NSW 2052, Australia

Corresponding authors: X. Zeng xqzeng@sjtu.edu.cn; X. Guo guoxianglong@sjtu.edu.cn; M. Huang mxhuang@hku.hk;

**Abstrac**t: The fretting corrosion testing of A690 with a sliding amplitude of 100 μm and a normal force of 20 N was conducted in a manually designed equipment with a tube-on-plate contact configuration exposed to simulated pressurized water reactor (PWR) secondary water. While A690 exhibits superior corrosion resistance, the fretting wear results in a two orders of magnitude faster oxidation rate at the contacting surface. A detailed characterization reveals that the fretting wear-induced dynamic stress/strain does not only constantly break the integrity of the oxide scale but also accelerate the consumption of Cr in the near-surface metal matrix. The degradation of corrosion resistance of A690 under fretting wear can be mainly attributed to 1) the decrease of oxide scale thickness; 2) the introduction of nanocavities and nano-cracks at the grain boundaries of the oxide scale; 3) the formation of a nano-grained Cr-depleted matrix zone under the oxide scale. These findings suggest that, for the structural alloys serviced at elevated temperatures, even a small amplitude motion with low normal stress against their contacting surface could significantly deteriorate their corrosion resistance. Hence, the service lifetime of the structural alloys needs to be reconsidered once friction is existing.

**Key words:** Ni-based alloy; Corrosion; Fretting wear; Dynamic stress/strain; Structure integrity.

## 1. Introduction

To reduce the emission of $CO_2$, nuclear power has been selected as one of the most promising substitutional energies of fossil fuel [1]. Currently, most of the in-service nuclear reactors are Gen-II and Gen-III [2], with Gen-IV nuclear reactors being actively developed by various institutes to further improve the safety and thermal efficiency [3-7]. As one of the most widely constructed nuclear reactors, PWRs are expected to prolong their lifetime from 40 years to 60 years, or if possible, to 80 years [8]. For this purpose, it is critical to preserve the integrity of the structural components in the harsh PWR environments during the prolonged operations.

Among the variety of structural components in PWRs, the normal operation of steam generators (SGs), which are primarily responsible for the heat exchange between the primary and secondary circuits and isolating the radioactive products from the primary to the secondary circuits, is directly related to the safety of the nuclear power plants [9]. The service environment for the SG tubes is exceptionally harsh, mainly due to high temperature, high stresses, and severe chemical corrosion [2]. Compared with ferritic/martensitic and austenitic stainless steels, Ni-based alloys tend to have much better corrosion resistance in high-temperature aqueous environments [5]. Consequently, the SG tubes were initially made of Ni-based 600 alloy (Ni-16Cr-7Fe) and then replaced by Ni-based A690 (Ni-30Cr-10Fe) due to the severe stress corrosion cracking (SCC) of 600 alloy after a relatively short service time [10-12]. The content of Cr was increased to ~30 wt.% in A690 to improve its corrosion resistance in the high-temperature water, as a result, obtaining an excellent SCC resistance. To date, the high-Cr Ni-based A690 has exhibited much better in-service SCC resistance than 600 alloy and no incidence of SCC of A690 has been reported in PWRs in service in either primary or secondary circuits since its first use in the late 1980s [10-12]. Consequently, A690 has been widely believed to be immune to SCC-induced failures in PWRs [8, 13].

Besides SCC, the small amplitude oscillatory motion of the SG tubes against the support plates, due to the flow-induced vibration (FIV), will lead to fretting wear at contacting surfaces between SG tubes and anti-vibration bars (AVBs) [2, 9]. Furthermore, the corrosion resulted by the high-temperature and high-pressure water in the secondary circuit will aggregate these damages together with the fretting wear. The simultaneous occurrence of fretting wear and corrosion, also named as fretting corrosion, is very common among the SG tubes, and such failures are difficult to overcome and avoid due to the lack of mechanistic understanding of loss of corrosion resistance under fretting corrosion conditions. A survey conducted by Dow [14] reported that many fretting-induced leaks occurred on the SG tubes in around 60 PWRs from 1992 to 1993. In addition, Hwang et al. [15] also found severe fretting corrosion related damages in Korean nuclear power plants. Moreover, such damages caused an unexpected shutdown in San Onofre Nuclear Generating Station Unit 3 in 2012 [16].

To alleviate the fretting corrosion related damages of SG tubes, many research efforts have been paid on the studies of the degradations of SG tubes under different conditions. However, the complicated environment in nuclear reactors complicates the study of fretting corrosion of SG tubes. In PWRs, the outer surfaces of the SG tubes and the AVBs are exposed into the secondary water, in which the temperature ranges from 270 to 290 °C, the pressure is ~6.7 MPa, and the pH value ranges from 9.5 to 10 [9, 17]. According to the experimental environments, the current research about the fretting corrosion of SG tubes can be mainly divided into four categories [2]: (a) Dry condition in air at room temperature [18-25]; (b) Dry condition in air at high temperatures [26-30]; (c) Water condition at room

temperature [31, 32]; (d) High-temperature and high-pressure water condition [17, 28, 33-41]. Although all these research works have significantly advanced our understanding of the fretting corrosion behaviors of SG tubes, the SG tubes, in practical conditions, are always serviced in the high-temperature and high-pressure secondary water environment, which could introduce different types and/or extents of corrosion compared with those tested in other environments [8, 13]. As a result, the experiments conducted in air/water at room temperature may simplify the influence of the corrosion on the degradation of SG tubes. Also, the corresponding conclusions may not be applicable to the SG tubes operated in PWR secondary water. For example, it is found that the worn scars formed on A690 tubes in water at room temperature are completely different from that in water at high temperature (285 °C) [17]. The oxide scale formed on the worn scar in room-temperature water was loose with clear cracks, while it was compact in high-temperature water, which indicated different fretting corrosion mechanisms of A690 in water at room temperature and high temperature. Hence, to obtain a more reliable understanding of the degradation of SG tubes caused by the fretting corrosion in the operating condition, it is necessary to conduct the experimental testing in a simulated secondary water environment.

A comprehensive understanding of the underlying mechanisms controlling the fretting corrosion of A690 in the simulated nuclear reactor environment is critical to avoid/alleviate fretting corrosion-induced leaks in SG tubes. To date, a thorough understanding of the degradation of corrosion resistance of A690 in a simulated secondary water environment is still largely lacking due to the difficulties in collecting the requisite experimental scale of observations (micro-to-atomic) on the fretting corrosion damage zones, although the studies on this topic are progressing in recent years [17, 28, 33-41]. Recent advances in high-resolution microscopic techniques, which allow for a more detailed characterization of material microstructures, have greatly advanced our understanding of a variety of previously unsolved phenomena [42-47]. Here, we undertake a fundamental study on the cross-sections of A690 tubes after the fretting corrosion testing using characterization techniques that span a number of length scales. The unprecedented micro-to-nano scale observations obtained in this study shed light on the underlying mechanisms controlling the accelerate corrosion of high Cr corrosion-resistant Ni-based alloys.

## 2. Experimental

The SG tubes used in this study were commercial nuclear grade A690 with a length of 16 mm, and inner and external diameters of 15.5 and 17.5 mm, respectively. 405 stainless steel (405 SS) was used as the AVB specimen, with a plate shape with dimensions of $7.6 \times 12.2 \times 3$ mm$^3$. The chemical compositions are listed in Table 1. Fig. 1 shows the electron backscattered diffraction (EBSD) images of the cross-section of A690 tubes. It is seen that the average grain size of A690 was ~70 μm. The microstructure of 405 SS was not examined in this study and it was reported to have a ferritic structure with an average grain size of 50 μm [37]. All the specimens were ultrasonically cleaned with deionized water and then dried with hot air before and after fretting corrosion tests.

Table 1 Chemical compositions of the materials used in this study (wt.%)

| Materials | C | Cr | Fe | Si | Mn | P | S | Al | Ni |
|---|---|---|---|---|---|---|---|---|---|
| A690 | 0.023 | 30.3 | 9.6 | 0.30 | 0.23 | 0.008 | 0.002 | 0.25 | Bal. |
| 405 SS | 0.056 | 12.5 | Bal. | 0.60 | 0.58 | 0.025 | 0.013 | 0.15 | 0.50 |

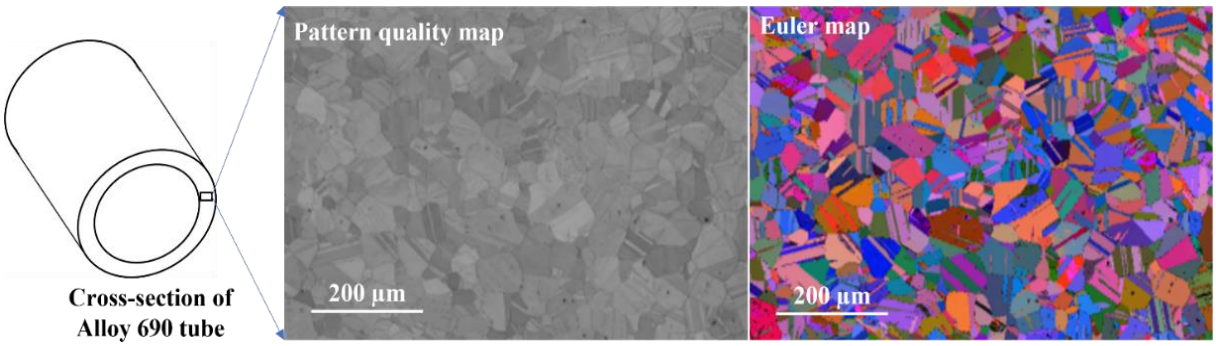


Fig. 1. EBSD analysis of the A690 tube before the testing (step size= 0.5 µm).

The fretting corrosion testing was conducted in a manually designed equipment with a tube-on-plate contact configuration inside an autoclave (Fig. 2a). The autoclave was connected to a water chemistry control loop [37] to maintain a simulated secondary water chemistry of PWR. The temperature, pressure, dissolved oxygen (DO), and pH of the secondary water were set as 285 °C, 8.6 MPa, no more than 5 ppb, and 9.75, respectively. The axial direction of A690 tube was parallel to the horizon and perpendicular to the fretting direction (Fig. 2a). The normal force and sliding amplitude were controlled to be 20 N and 100 µm, respectively, which were chosen based on the practical operating conditions of the SG tubes [17, 48]. The fretting frequency and total cycles were set to be 5 Hz and 500000, respectively. The total fretting corrosion time was ~28 h. It is noted that each test was repeated for at least 4 times and the corresponding results were averaged to ensure the accuracy in this study.

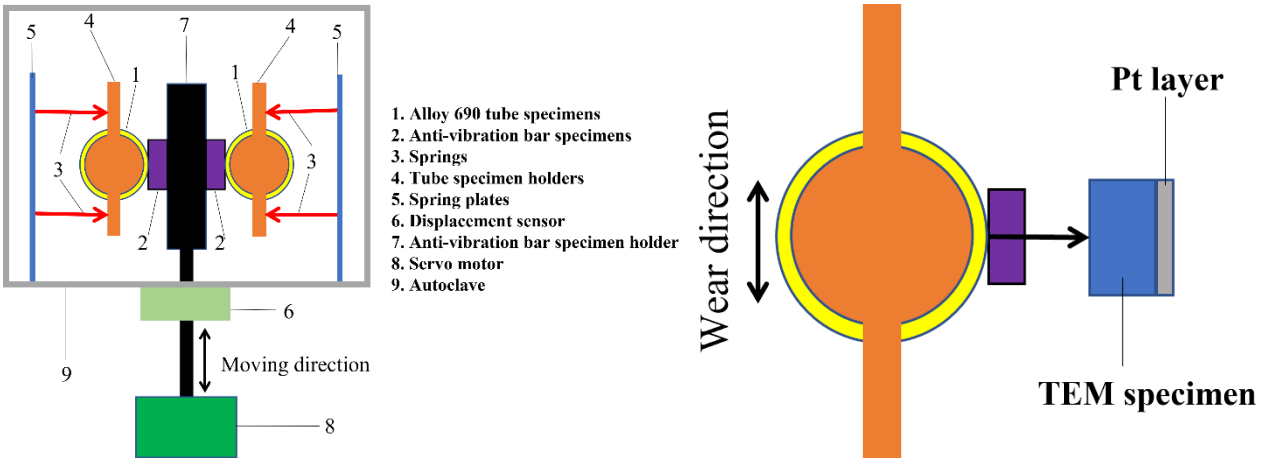


(a) (b)

Fig. 2. Schematic diagram showing (a) the experimental equipment for the fretting corrosion testing and (b) the orientation of the TEM foils relative to A690 tube.

The surface morphology of A690 tubes after fretting corrosion tests was analyzed using a Zeiss Merlin scanning electron microscope (SEM). A 3-dimensional optical microscope (OM, Bruker ContourGT-1) was used to measure the wear volumes. Thin foils were prepared from A690 tubes after exposure by a dual-beam Zeiss Nvision 40 focused ion beam (FIB), which orientations are shown in Fig. 2b. The microstructure was analyzed by an aberration-corrected JEOL ARM200F transmission electron microscope (TEM), while the compositions and elemental distributions were detected by an electron energy loss spectroscopy (EELS) detector. Relative errors in EELS quantification were dominated by uncertainties in theoretical cross-sections and can be assumed to be ~10% for most measurements. A Zeiss Merlin SEM equipped with an on-axis transmission Kikuchi diffraction (TKD) detector was used

for crystallographic analysis of the thin foils.

## 3. Results

### *3.1 OM and SEM analysis*

After the fretting corrosion testing in the simulated secondary water of PWR, a 3-dimensional OM was used to measure the volumes of the worn scars. The representative 3-dimesional profile micrograph is shown in Fig. 3a. The averaged wear volume and depth of the worn scars were measured to be ~3.49× $10^6$ μm$^3$ and ~2.6 μm, respectively. The wear coefficient can be calculated based on the Archard equation [49-51]:

$$V=KFS \quad (1)$$

where $K$ is the wear coefficient, $V$ is the wear volume, $F$ is the normal force, and $S$ is the sliding distance. The calculated wear coefficient was 0.88 × $10^{-3}$ μm$^2$/N. The representative SEM morphologies of the worn scars are shown in Fig. 3b. The surface of the worn scars was generally smooth. Many grooves were observed on the surface of the worn scars, and these grooves were parallel to the wear direction. Nearly no craters were observed on the surface of the worn scars, while a large number of detachments were observed, indicating a delamination wear mode [2, 9]. Oxide debris was occasionally observed on the worn scar surface, and the size was smaller than 100 nm. The representative SEM morphologies of the unfretted surface are shown in Fig. 3c. It is seen that the surface which was free of fretting wear had been oxidized during the fretting wear testing and was uniformly covered by discrete oxide particles. These oxide particles were widely reported as Fe-rich spinel oxides [2, 9].

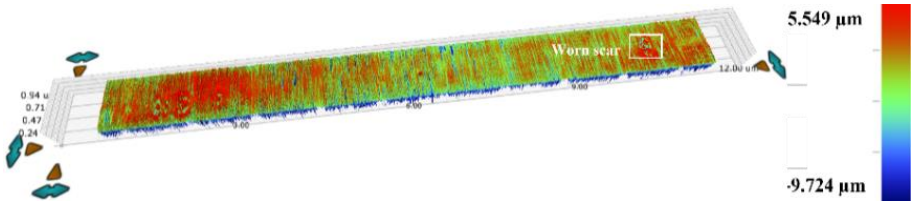


(a)

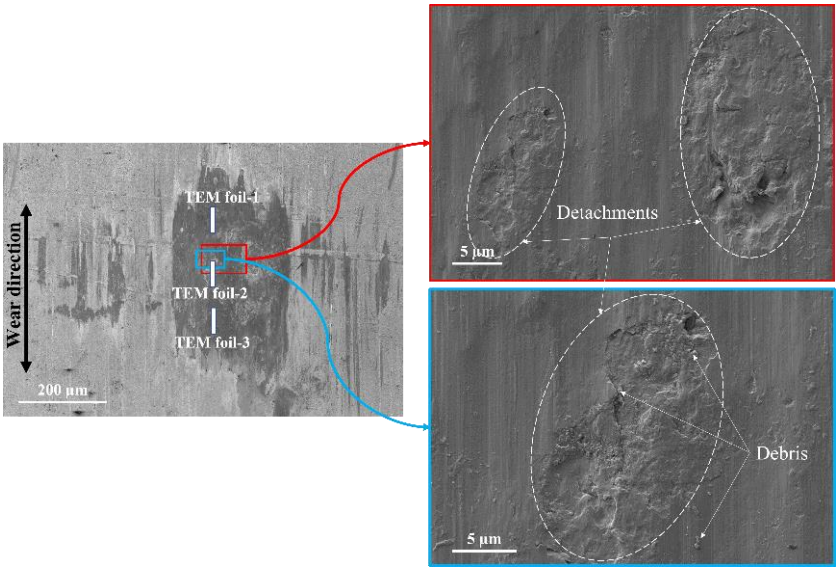


(b)

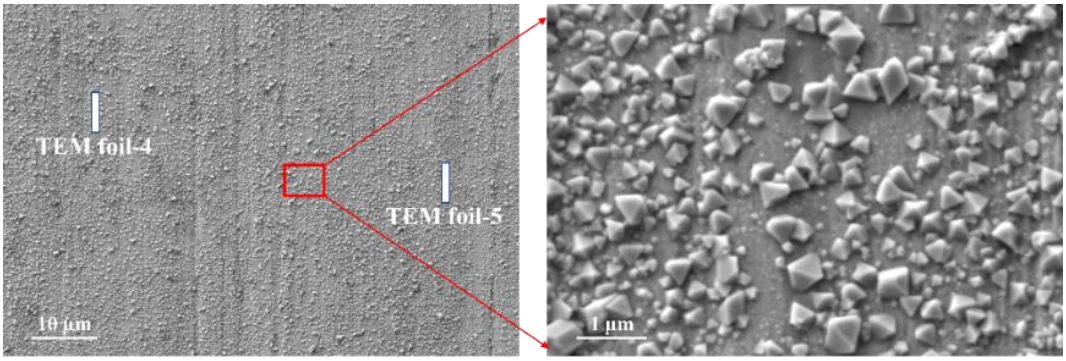


(c)

Fig. 3. (a) The 3D-profile micrographs of the worn scars on A690; SEM-SE images showing the surface morphologies of the (b) worn scars and (c) unfretted surface.

*3.2 TEM/EELS analysis*

To study the effect of fretting wear on the corrosion of A690, three TEM foils (TEM foil 1-3, Fig. 3b) were prepared from the worn scar and two TEM foils (TEM foil 4-5, Fig. 3c) were prepared from the unfretted surface. The positions of these TEM foils are highlighted by the white rectangles (Figs. 3b and c). The TEM foils prepared from the unfretted surface only experienced corrosion during the testing. They were used to compare with those prepared from the worn scars, which experienced corrosion and fretting wear simultaneously during the testing. The orientations of the site-specific TEM foils relative to A690 tube are shown in Fig. 2b. After the TEM foils were thinned to a thickness of ~50 nm, the morphologies of the TEM foils were preliminarily examined by SEM-InLens/SE imaging. The representative SEM-InLens and SEM-SE images of the TEM foils prepared from unfretted surface and worn scar are shown in Figs. 4a and b, respectively. The oxide and metal matrix can be distinguished by the different image contrasts. The surfaces of the worn scars and the interfaces between the oxide and metal matrix are highlighted by the yellow dashed lines.

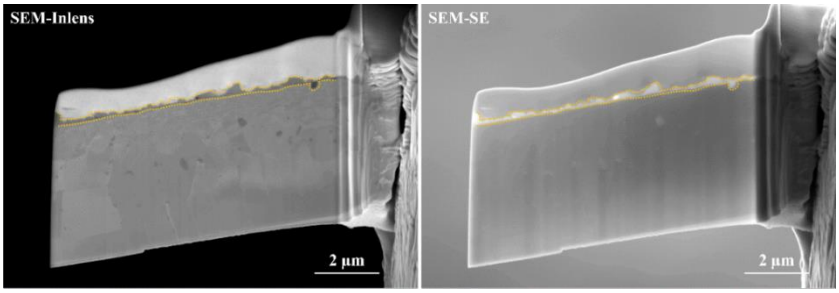


(a)

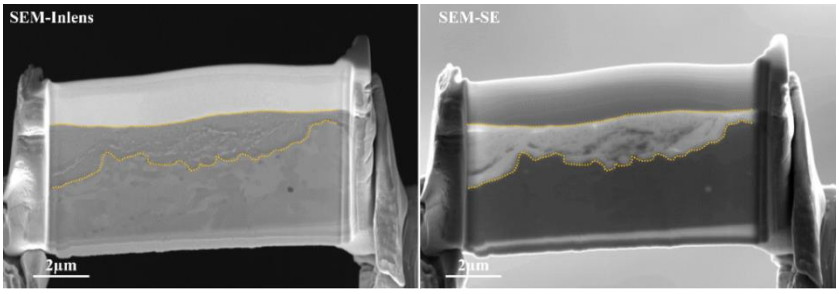


(b)

Fig. 4. The representative SEM-InLens/SE morphologies of the TEM foils prepared from (a) the unfretted zone (TEM foil-4) and (b) the worn scar (TEM foil-1).

*3.2.1 Corrosion of A690 without fretting wear*

To study the corrosion of A690 without fretting wear in the secondary water, high-angle annular dark field (HAADF) and bright field (BF) imaging were conducted to examine the cross-section of A690, as shown in Fig. 5. In the HAADF and BF images, the oxide and the metal matrix can be easily distinguished due to their different image contrasts. It can be seen that the oxide scale was very thin, with an average thickness of ~10 nm. The discrete surface oxide particles observed on the outer surface (Fig. 3c) were also observed in Fig. 5. The diffraction contrasts in the BF images show that there was a nano-grained matrix layer with a thickness of about 1 μm under the surface oxide scale.

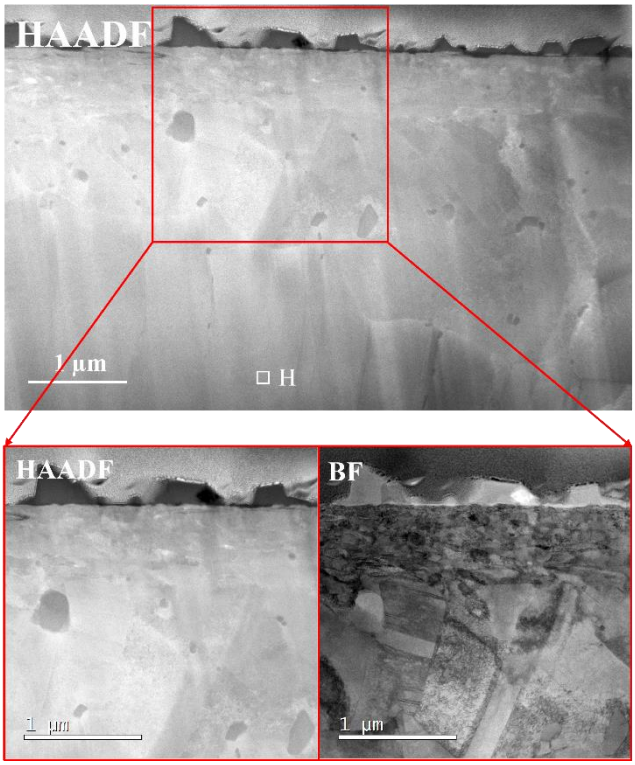


Fig. 5. The HAADF and BF images showing the morphologies of the cross-section of A690 without fretting wear after the fretting corrosion testing.

To examine the chemical composition of the oxide scales, EELS mapping was conducted. Fig. 6a shows a cross-section of a region where the inner oxide scale had no outer surface oxide particles above. As can be seen, the thin oxide scale was mainly enriched in Cr. The representative chemical composition measured from Region A was 55% Cr, 6% Fe, 3% Ni, and 36% O. Hence, the thin oxide scale was very likely to be composed of $Cr_2O_3$. Fig. 6b shows the cross-section of the inner oxide scale where it was covered by an outer surface oxide particle. The chemical composition of the thin inner oxide scale (Region B) under the outer oxide particle was similar to that of Region A. The chemical composition of the outer oxide particle (Region C) was 55% O, 1% Cr, 29% Fe, and 15% Ni, which is very likely to be $NiFe_2O_4$. It is worth noting that the matrix under the inner oxide scale was not effectively protected since discrete Cr-rich oxide precipitates were observed, suggesting internal oxidation might have occurred. The chemical composition measured from the specific regions are summarized in Table 2.

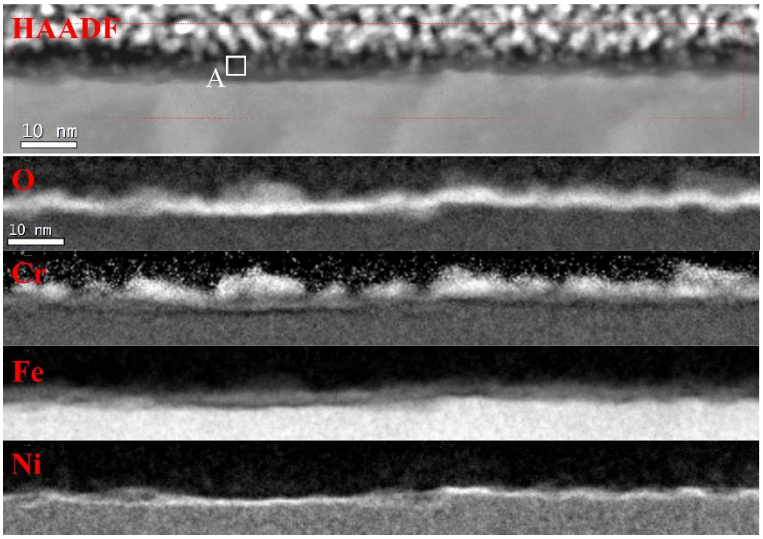


(a)

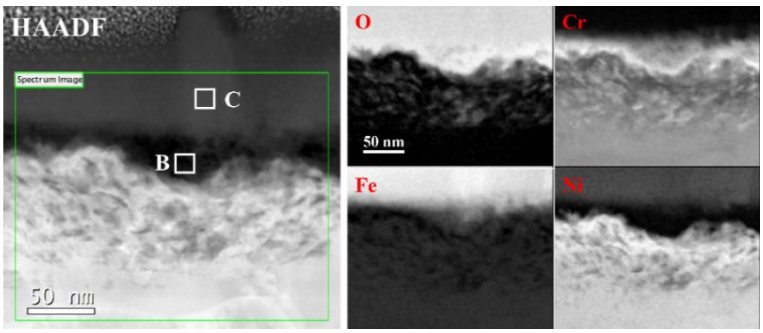


(b)

Fig. 6. HAADF images and related qualitative EELS chemical composition maps showing the elemental distribution of O, Cr, Fe, and Ni of A690 without fretting wear: (a) surface oxide zone without oxide particle and (b) surface oxide with oxide particle.

Table 2 Site-specific chemical compositions measured by EELS.

| Regions | Composition (at. %) | | | |
|---|---|---|---|---|
| | O | Cr | Fe | Ni |
| A | 36 | 55 | 6 | 3 |
| B | 37 | 53 | 9 | 1 |
| C | 55 | 1 | 29 | 15 |
| D | 56 | 15 | 19 | 10 |
| E | 0 | 18 | 8 | 74 |
| F | 0 | 21 | 9 | 70 |
| G | 0 | 27 | 9 | 64 |
| H | 0 | 32 | 10 | 58 |

*3.2.2 Corrosion of A690 with fretting wear*

Fig. 7 shows the HAADF and BF images of the cross-section of A690 prepared from the worn scar, where no obvious inner and outer oxide layers are observed. The average thickness of the oxide scale was ~2.5 μm, which was higher than that formed on the surface without fretting wear (Fig. 6). Further observation shows the existence of metallic phase. The shapes of the metallic phase were irregular, and the sizes ranged from several nanometers to several microns. In addition, a crack was observed in the oxide scale. The BF images show that the metal matrix under the oxide scale was composed of nano-sized grains. The metal phase in the oxide scale also appeared to consist of nano-sized grains.

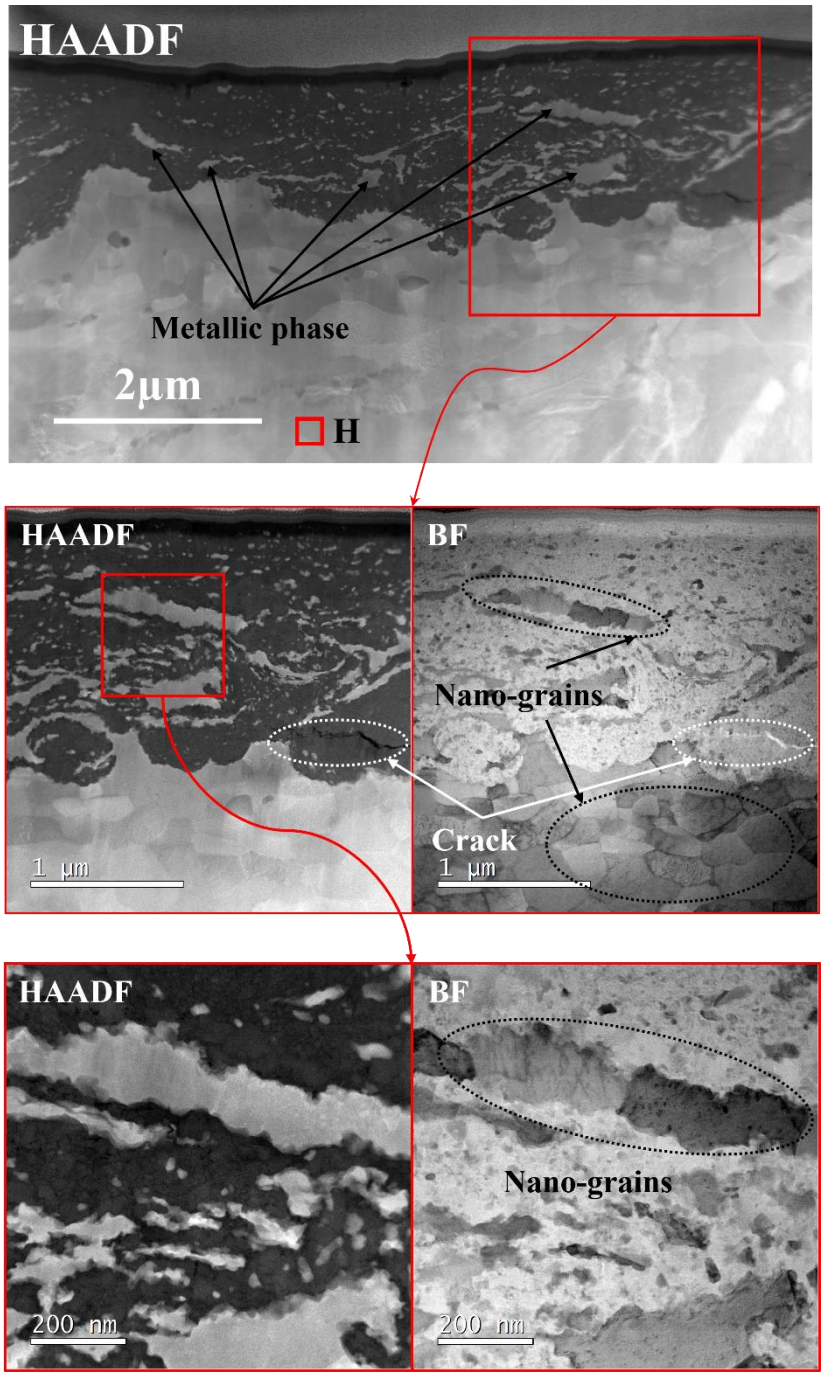


Fig. 7. The HAADF and BF images showing the morphologies of the cross-section of A690 with fretting wear after the fretting corrosion testing.

The chemical composition distribution on the cross-section of A690 prepared from the worn scar was analyzed by EELS. The HAADF image and the corresponding EELS chemical composition maps are shown in Fig. 8a, in which the oxide was enriched with Fe and depleted in Cr and Ni. Based on the data from the spot analysis, the oxide in Region D seemed to be Cr- Fe-Ni spinel (57% O, 13% Cr, 19% Fe, and 11% Ni). The metal phase in Region E was composed of 25% Cr, 6% Fe, and 69% Ni. Besides, Cr in Region F was much lower than that in the original metal matrix (Region H, Fig. 7). In addition, Cr-rich carbides were observed in the matrix and expected to have formed before the ferreting corrosion tests. The HAADF image and the corresponding EELS chemical composition maps around the oxide/matrix interface are enlarged in Fig. 8b. A large number of nano-sized metallic particles, mainly composed of Ni, were observed. The elemental distribution across the oxide-metal matrix interface was revealed by an EELS line-scan, as shown in Fig. 8d. It is seen that the chemical compositions in the oxide scale and the metal matrix under the oxide scale were not uniform. The Cr content in the matrix decreased towards the oxide scale, suggesting that Cr was depleted in the near-surface metal matrix. The content of Ni in the near-surface matrix showed an opposite trend, while the content of Fe nearly remained constant. Further observation shows that the oxide scale consisted of nano-sized oxide grains (Fig. 9c), and a large number of nanocavities and nano-cracks were observed at the grain boundaries of nano-sized oxide, as highlighted by dashed circles.

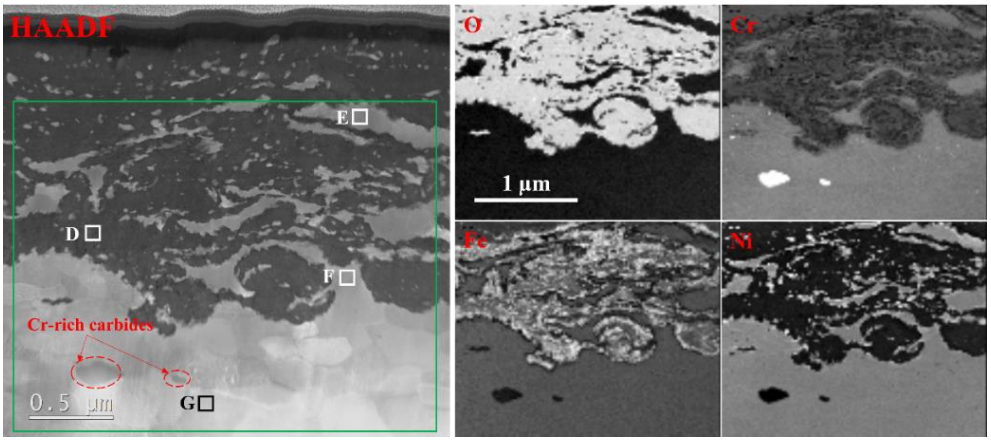


(a)

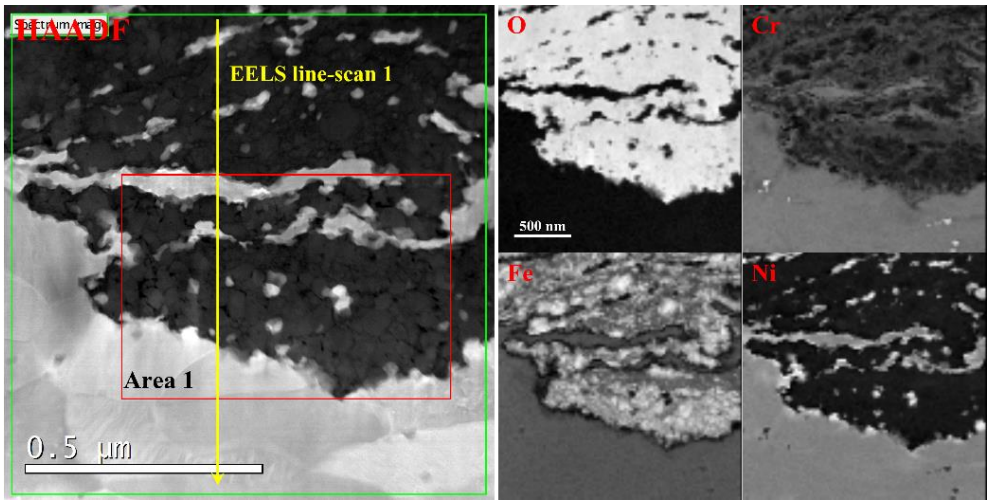


(b)

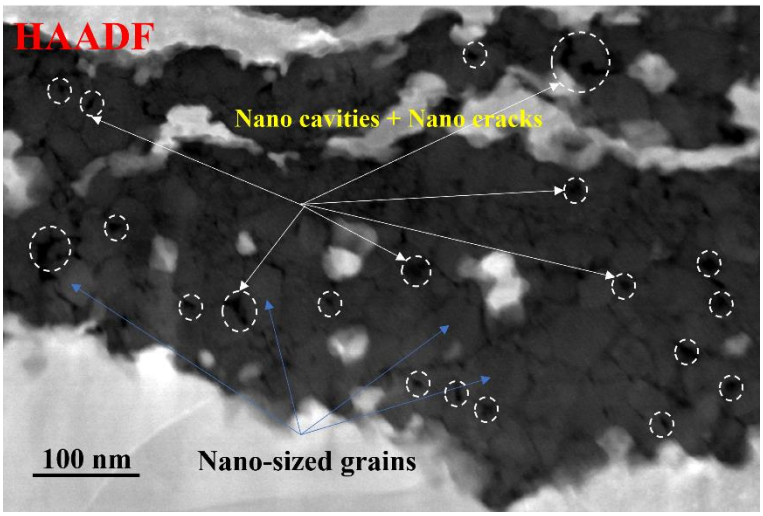


(c)

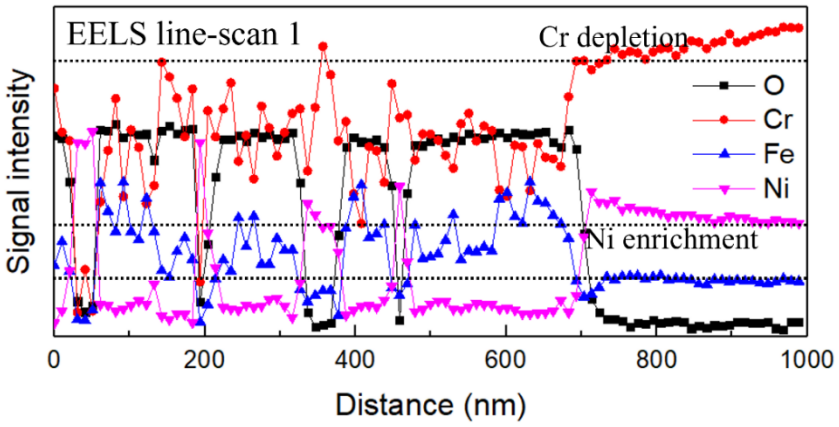


(d)

Fig. 8. (a) HAADF image and related qualitative EELS chemical composition maps; (b) higher resolution HAADF image and related qualitative EELS chemical composition maps; (c) magnified HAADF image of Area 1; (d) EELS line-scan showing the qualitative chemical composition distribution of O, Cr, Fe, and Ni.

*3.3 TKD analysis*

The cross-section of A690 without fretting wear was analyzed by on-axis TKD. According to the different image contrasts, the forward scatter detector (FSD) image in Fig. 9a can distinguish the surface oxide and the metal matrix, and the oxide/metal matrix interface is considered as the original surface of the specimen, as highlighted by a white dashed line. The thickness of the surface oxide scale was ~10 nm. Furthermore, it shows a nano-grained layer under the original surface and a plastic deformation layer with many deformation bands, as pointed out by the black arrows, under the nano-grained layer. The nano-grained layer/plastic deformation layer interface is highlighted by a yellow dashed line. The position of the interface is mainly identified based on the morphology of the grain shape. The pattern quality map in Fig. 9b and the inverse pole figure (IPF) maps in Fig. 9d shows clearer images. Moreover, the detailed morphologies of the nano-grained layer are shown in a magnified grain shape map, as shown in Fig. 9e. The size of the grains was not uniform ranging from less than 10 nm to 500 nm and much smaller than the average size of A690 (70 μm, Fig. 1). Fig. 9c

shows the distribution of different phases in the cross-section. The metal matrix, Cr-rich carbide and oxide are indexed as austenite, $Cr_{23}C_6$, and spinel, respectively. The austenite and spinel cannot be distinguished effectively by TKD because of the similar crystallographic structure, as shown in Fig. 9c.

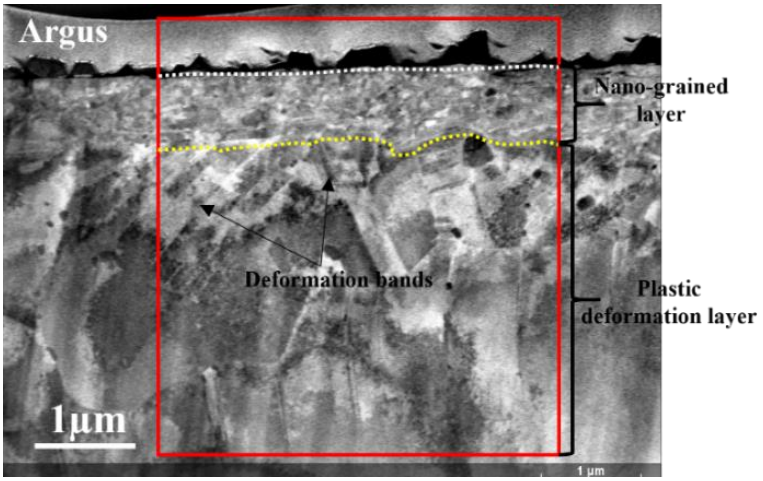


(a)

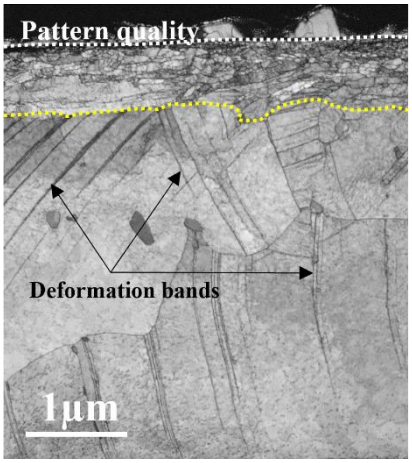


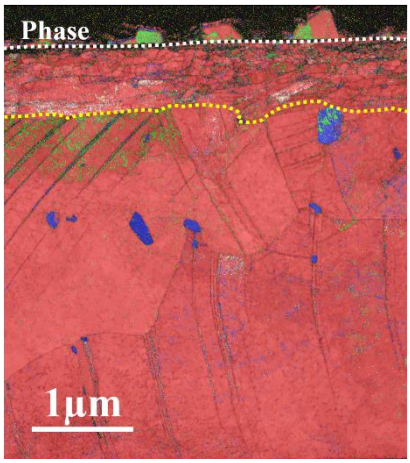


(b) (c)

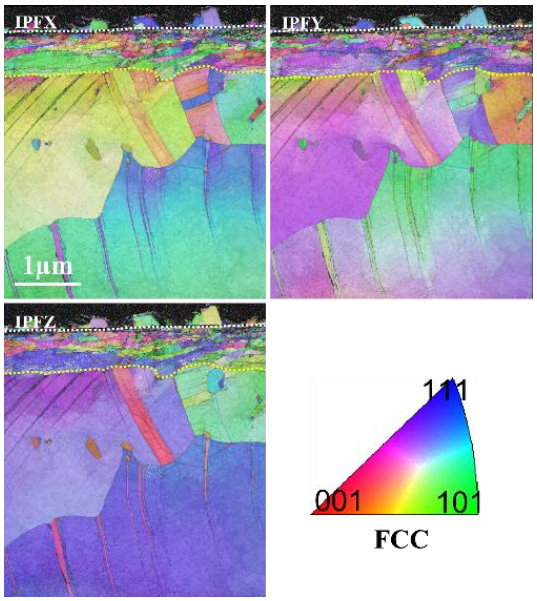

(d)

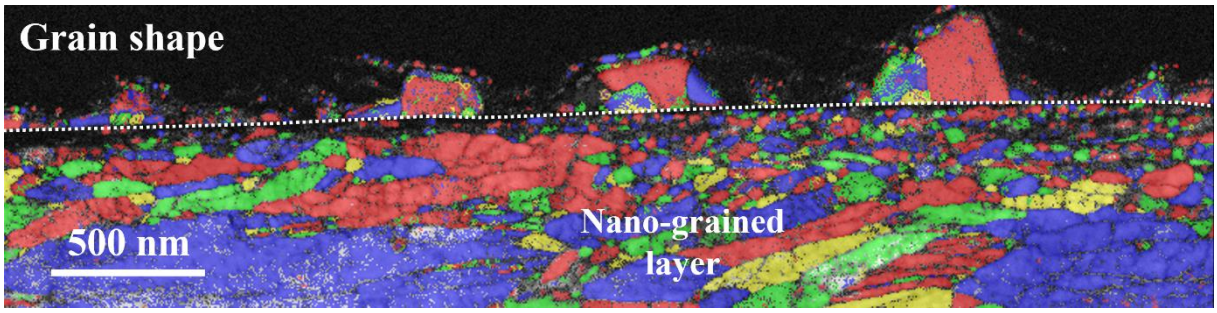


(e)

Fig. 9. TKD analysis on the cross-section of A690 without fretting wear after the fretting corrosion testing (step size=3 nm, collected Kikuchi pattern resolution=800 × 1200). (a) FSD map; (b) pattern quality map; (c) phase map (austenite in red, spinel in green, $Cr_{23}C_6$ in blue); (d) IPF maps with orientation legend of FCC phase; (e) magnified image showing the distribution of grain shapes.

Fig. 10a shows the FSD image of the cross-section of A690 prepared from the worn scar. It is seen that a metal phase existed in the oxide scale, and a nano-grained layer and a plastic deformation layer under the oxide scale. The surface of oxide scale is highlighted by a white dashed line, the oxide scale/metal matrix interface is highlighted by a red dashed line, and the nano-grained layer/plastic deformation layer interface is highlighted by a yellow dashed line. The different features can also be observed in the pattern quality map (Fig. 10b) and the IPF maps (Fig. 10d). The size of grains in the nano-grained layer increased from ~200 nm to ~800 nm along the direction towards the matrix (Fig. 10b). Fig. 10c shows the phase distributions on the cross-section. Although the spinel oxide and the austenite metal cannot be effectively distinguished, the FSD image can be combined with the phase map to identify the positions of the oxides. $Cr_{23}C_6$ carbides were also observed in the matrix. The enlarged IPFZ image (Fig. 10e) shows that the oxide scale was composed of nano-sized grains (less than 100 nm), which is consistent with the results in Fig. 8c.

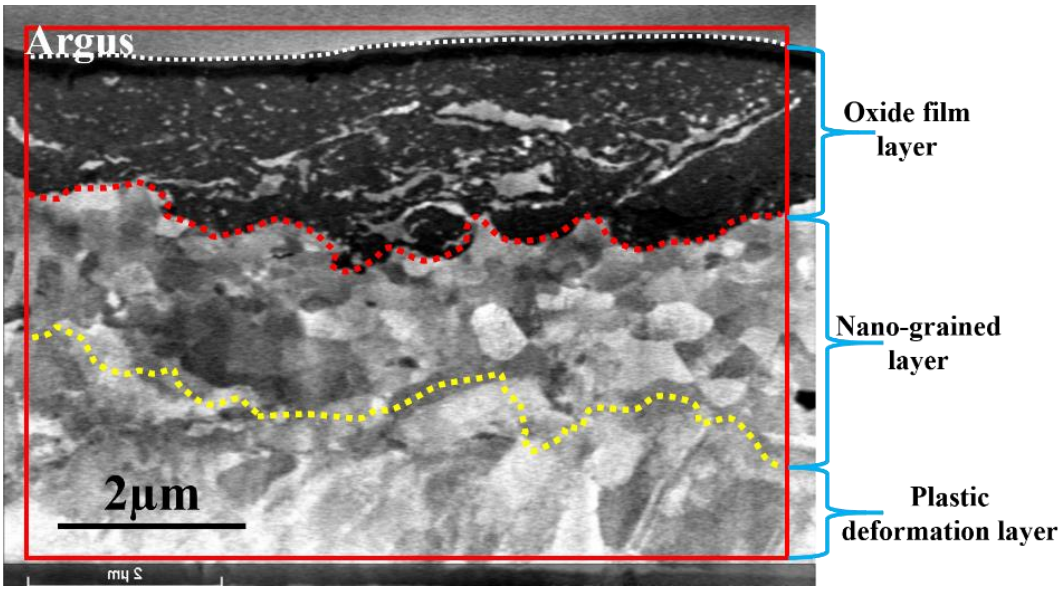


(a)

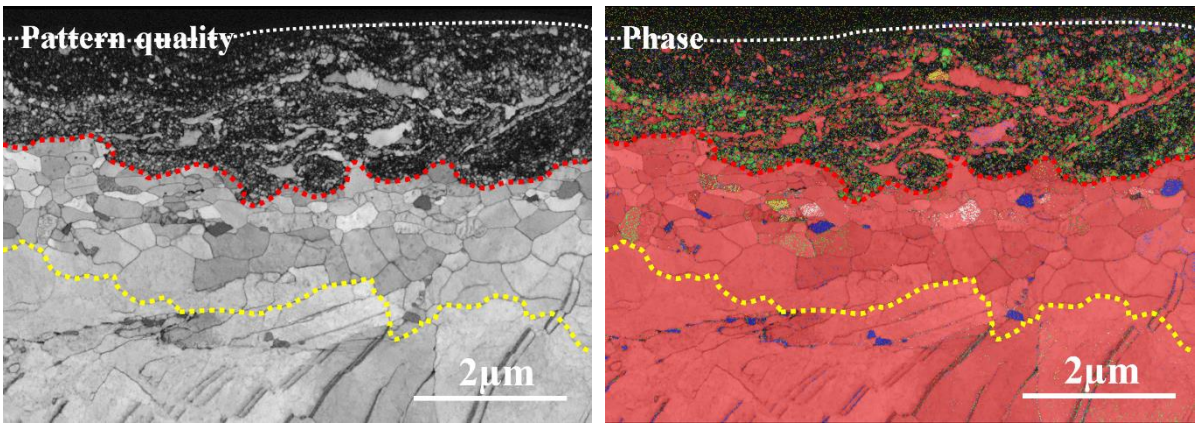


(b)




(c)

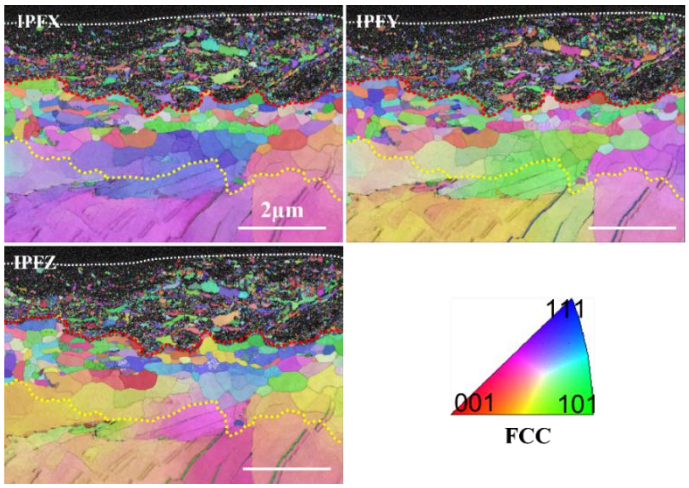


(d)

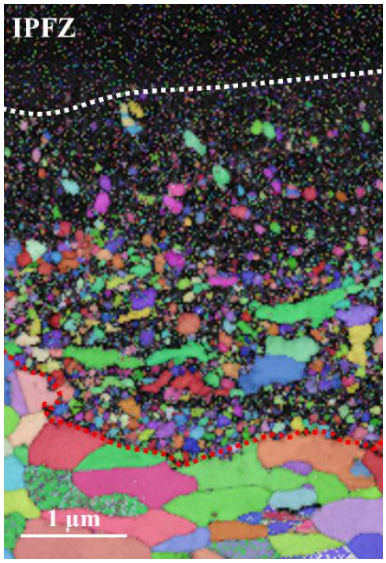


(e)

Fig. 10. TKD analysis on the cross-section of A690 with fretting wear after the fretting corrosion testing (step size=3 nm, collected Kikuchi pattern resolution=800 × 1200). (a) FSD map; (b) pattern quality map; (c) phase map (austenite in red, spinel in green, $Cr_{23}C_6$ in blue); (d) IPF maps with orientation legend of FCC phase; (e) magnified IPFZ image.

## 4. Discussion

*4.1 The high-temperature water corrosion of A690 without fretting wear*

The high-temperature water is normally reported to endanger the long-term safe running of the structural materials used in the nuclear reactors due to the corrosion-related degradations. The corrosion of A690 in the nuclear reactor environment has been extensively studied [11-13, 52-54]. It is generally reported that this alloy has superior corrosion resistance in the high-temperature water due to its over 30 wt.% of Cr content in the matrix, which could facilitate the formation of a compact chromia oxide scale on the surface to protect the alloy from further oxidation [11-13, 52-54]. The superior corrosion resistance of this alloy was attributed to the formation of a super thin surface oxide scale, which is normally less than 20 nm [13, 52-54]. This will inevitably increase the technical difficulty in analyzing the oxide scale formed on this alloy and prevent the mechanistic understanding of the corrosion of this alloy in the high-temperature water. In addition, A690 studied in literature has always been well-polished to remove the cold-worked sublayer caused by the process of sample preparation [13, 52-54]. However, the A690 SG tubes used in the nuclear reactors always have a cold-worked sublayer caused by the process of manufacturing. Hence, the results obtained from the well-polished A690 may not be representative to the in-service performance of A690 SG tubes.

The A690 used in this study was prepared from the commercial nuclear grade A690 tubes. No further treatment was conducted on this alloy before the testing. Hence, the results obtained from the present study could be more representative to the in-service performance of A690 SG tubes. As shown in Figs. 5 and 9, a nano-grained sublayer can be observed under the unfretted surface. The thickness of this sublayer was not uniform, about 1 μm on average. This sublayer is believed to be formed during the process of manufacturing. The ununiform thickness of the nano-grained sublayer suggests that the surface deformation during the manufacturing was not uniform either. The HAADF-EELS analyses show that the oxidation of the unfretted surface of A690 tube was also not uniform, and two representative cross-sectional regions can be observed (Figs. 6a and b). Fig. 6 shows the region which was covered by a thin Cr-rich oxide scale (~ 10 nm). A relatively thicker oxide scale is also observed in Fig. 6b, while the metal matrix was not effectively protected since internal oxide precipitates were observed in the metal matrix under the oxide scale.

The internal oxidation was believed to be unable to occur at the PWR operating temperatures until a recent work conducted by Shen et al. [55], in which the internal oxidation occurred in a 20% cold-worked 316 stainless steel (316 SS) after oxidized in 340 °C high-temperature water but not in a 0% cold-worked 316 SS. These authors proposed that although the cold work could enhance the outward diffusion of Cr and facilitate the formation of a compact Cr-rich oxide scale, the inward diffusion of oxygen could also be accelerated simultaneously due to the existence of high-density defects in the cold-worked matrix. If the inward diffusion of oxygen is faster than the outward diffusion of Cr, the internal oxidation could occur. The results observed in Fig. 6 could be well explained by the theory proposed in [55]. The representative region in Fig. 6a was due to a faster outward Cr diffusion than the inward oxygen diffusion, resulting in the fast formation of a thin Cr-rich oxide layer and protecting the underneath metal matrix. However, the inward oxygen diffusion was faster than the outward Cr diffusion in Fig. 6b, which could allow the inward diffusion of oxygen into the metal matrix and lead to the occurrence of internal oxidation before the formation of a continuous Cr-rich oxide layer. Consequently, it is reasonable to believe that the ununiform deformation in the nano-grained layer

could result in different extent of surface oxidation at different regions (ununiform oxidation). The effect of surface state on the surface oxidation has also been studied by other researchers [55-59].

*4.2 Origin of the surface oxide scale on the worn scars of A690*

As shown in Fig. S1a, a TEM foil was prepared from the edge of the worn scar, which was covered by the oxide debris generated during the fretting corrosion testing. Fig. S1b shows that the interface between the oxide scale and metal matrix was quite flat, which corresponds with the original surface of A690 tube, confirming that the oxide scale was formed by the pile-up of the oxide debris from the surrounding fretting corrosion regions during the testing. The oxide debris was compressed by the AVB specimen during the testing to form a relatively compact oxide scale, which protected the localized metal matrix from fretting corrosion. The EELS elemental distribution maps show that the chemical composition of the oxide scale was not uniform (see Cr-map in Fig. S1b). This is mainly because the oxide debris came from the oxidation of A690 and 405 SS, and the oxidation of the two alloys with much different Cr contents (30.3 wt.% vs. 12.5 wt.%) would result in the formation of oxides with different Cr contents. The significant Cr fluctuations in the oxide scale could be explained by the mixture of the oxide debris with different Cr content from the two alloys, as seen in Fig. S1b. In addition, no metallic phases were observed in the oxide scale, which was different from the oxide scale formed on the worn scars (Figs. 7 and 8).

As to the origination of the surface oxide scales on the worn scars of A690, two possibilities are suggested. The first one is that it was formed by the pile-up of the oxide debris, similarly to that in Fig. S1. Since the oxide scale in Fig. S1 has been demonstrated to be formed by the pile-up of oxide debris, if the formation of the oxide scales on the worn scars (Figs. 7 and 8) was also due to the oxide debris pile-up, their microstructure and microchemistry should be similar. EELS analysis showed that the Cr distribution in the oxide scales formed on the worn scars was generally uniform (Cr-map in Fig. 8), which was different from that in Fig. S1b. Hence, the absence of significant Cr fluctuations in the oxide scale formed on the worn scars suggests that the formation of the oxide scales on the worn scars was not due to the oxide debris pile-up. Consequently, the first possibility can be ruled out. The second one is that it was formed by the accelerated internal oxidation of the metal matrix of A690. As shown in Figs. 7 and 8, a large number Ni-rich metallic phases existed in the oxide scales formed on the worn scars. All the metallic phases were indexed as austenite, corresponding to the residual metal matrix of A690. The co-existence of metallic phase and oxide phase in the oxide scale is a typical feature of internal oxidation, which was also observed in Alloy 600 with a cold-worked surface after oxidized in the simulated PWR primary water [55-57]. Internal oxidation had been observed on the area without fretting wear due to the prior near-surface deformation caused by the process of manufacturing (Fig. 6b). Compared with the surface without fretting wear, the internal oxidation under the surface with fretting wear was significantly accelerated. This is mainly because the fretting wear would not only continuously introduce deformation into the near-surface region but also introduce dynamic stress/strain into the oxide scale, breaking the compact structure of the oxide scale (and its protectiveness) and accelerating the oxidation of metal matrix.

*4.3 The effect of fretting wear on the loss of corrosion resistance of A690*

As shown in Fig. 7, the thickness of the oxide scale on the worn scars of A690 was ~2.5 μm, which was about 250 times thicker than that formed on the surface without fretting wear (~10 nm, Fig. 6). It is worth noting that the actual thickness of the oxide scale on the worn scars should be even thicker

since the fretting wear had led to the thinning of the oxide scales. The average depth of the worn scars of A690 was measured to be ~2.6 μm. If we assume that the formation of the worn scars was due to the thinning of the oxide scale, the total thickness of the oxide scale formed on the surface with fretting wear should be doubled. It suggests that the oxidation rate of A690 with fretting wear was over 500 times faster than the surface without fretting wear.

For alloys subjected to high-temperature environments, it is crucial to grow a continuous, slow growing, thermodynamically stable oxide scale, which works as a diffusion barrier [60]. To achieve this objective, a certain content of stable-oxide-forming elements such as Cr, Al, and Si, is required [61]. The minimum content of stable-oxide-forming elements is required for two reasons: 1) to achieve an external oxidation; and 2) to provide a diffusive flux of elements towards the oxide scale, to enable its sustained growth and reformation in case of exfoliation. If the content of the stable-oxide-forming elements is lower than this critical value, a protective oxide scale cannot form and internal oxidation may continue. For A690, the stable-oxide-forming element is Cr. Although localized internal oxidation was observed (Fig. 6b), a thin continuous Cr-rich oxide layer was formed on the whole surface of A690 without fretting wear, which indicates that the Cr content in this alloy was high enough for the occurrence of external oxidation. Hence, it is reasonable to attribute the loss of corrosion resistance of A690 during the fretting corrosion testing to the fretting wear between the contacted surfaces.

Most of the studies in literature about the fretting corrosion of A690 in high-temperature water were mainly focused on quantifying the wear value and characterizing the worn scar surface morphology [28, 34, 35, 37, 39, 40], but the high-resolution study on the cross-section of worn scars is rarely reported, which has been demonstrated to be an effective way of understanding the the mechanisms controlling materials degradations [17, 33, 36, 38]. The detailed high-resolution characterization analyses on the cross-sections of A690 with and without fretting wear in this work provided new insights into the mechanistic understanding of the loss of corrosion resistance of A690. On the one hand, the fretting wear would reduce the thickness of the oxide scale, and then reduce its blocking effect on ion diffusion. On the other hand, the dynamic stress/strain caused by the fretting wear would constantly break the integrity of the oxide scale by introducing a large number of nanocavities and nano-cracks into grain boundaries of the oxide scales (Fig. 8c). The oxide scale would then completely or partially loss its protectiveness, depending on the extent of damages caused by the fretting wear. More oxygen, as a result, would diffuse into the metal matrix and result in the fast thickening of the oxide scale.

The fretting wear would not only reduce the protectiveness of the oxide scale, but also change the microstructure of the near-surface metal matrix. As shown in Figs. 7 and 10, a nano-grained layer was observed just beneath the oxide film. Since the depths of the worn scars were larger than the original thickness of the nano-grained layer caused by manufacturing, the nano-grained layers observed in Figs. 7 and 10 are believed to be caused by the fretting wear during the testing. The fretting wear-induced mechanical deformation and nano-recrystallization in the near-surface metal matrix could accelerate the outward diffusion of Cr to the oxide scale due to the increased grain boundary density [55-59]. However, the enhanced outward diffusion of Cr would not necessarily result in the formation of a more compact surface oxide scale due to the dynamic stress/strain-induced nanocavities and nano-cracks in the oxide scale as mentioned above. The enhanced Cr outward diffusion would consume more Cr and result in more significant Cr depletion in the near-surface metal matrix. The Cr-depletion in the metal matrix and the dynamic stress/strain, as a result, would also accelerate the internal oxidation of A690.

*4.4 The effect of high-temperature water corrosion on the fretting wear of A690*

In a recent work conducted by Lai et al. [17], it is found that the wear volume of A690 in high-temperature water was much smaller than that in air at room temperature, under which the corrosion of A690 can be neglected compared with that in the high-temperature water. It indicates that although the fretting wear could accelerate the high-temperature water corrosion of A690, the high-temperature water corrosion, on the contrary, could inhibit its fretting wear [17]. The hardness of the oxides is generally greater than that of the metal matrix, which is believed to exhibit better wear resistance [62-66]. The relatively thick oxide scale formed in the high-temperature water, as a result, could work as a glaze layer and protect the underneath metal matrix from the fretting wear [17]. Hence, the decreased wear volume in the high-temperature water was attributed to the formation of an oxide scale in this corrosive environment [17]. The high-temperature water corrosion is always detrimental to the service performance of the structural materials. However, the oxide scale formed in this environment could significantly improve their fretting wear performance.

*4.5 Current understanding of the fretting corrosion on the degradation of A690*

The fretting corrosion-induced degradation of A690 tubes in the PWR secondary water has been demonstrated to be the synergistic effect of high-temperature water corrosion and fretting wear. According to the results reported in this study and in literature [17, 28, 33-41], a detailed description of the synergistic effect of high-temperature water corrosion and fretting wear on the degradation of A690 is proposed in Fig. 11. Prior to the fretting corrosion testing, the manufacturing process introduced a nano-grained layer and a plastic deformation layer under the surface of A690 tubes. Once the A690 tube is exposed to the high-temperature water, the increased grain boundary density in the nano-grained layer enhances the outward Cr diffusion, resulting in a rapid formation of a Cr-rich oxide scale with locally internal oxidation, as shown in Fig. 11a. Although the initially formed Cr-rich oxide scale is superior protective, the dynamic stress/strain caused by the fretting wear between A690 tube and the AVB specimen constantly breaks the integrity of the Cr-rich oxide scale by introducing nanocavities and nano-cracks in the oxide scale, which will inhibit the occurrence of external oxidation and accelerate the internal oxidation. With the increase of the testing time, the oxide scale thickens due to the accelerated internal oxidation while the fretting wear is simultaneously reducing the thickness of the oxide scale. At the same time, more and more Cr in the near-surface metal matrix is consumed in the healing of the surface oxide scale, resulting in the formation of a Cr-depletion zone under the oxide scale. Hence, the contacting surface of A690 tube will suffer a rapid internal oxidation during the entire experimental period. Due to the greater hardness of the oxide in comparison with the metal matrix, the formation of an oxide scale on the worn scars will increase the fretting wear resistance of A690 tube. Although the fretting wear resistance of A690 tube is increased by the formation of an oxide scale, the oxide scale is not immune to the fretting wear-induced damages. The fretting wear between A690 tube and the AVB specimen will not only introduce defects into the oxide scale, but also decrease its total thickness, resulting in an enhanced internal oxidation. Although the oxide scale on the surface of the worn scars prevents the direct contact of the metal matrix of A690 tube and the AVB specimen, the fretting wear between them can still mechanically change the microstructure of the underneath metal matrix, resulting in the formation of a nano-grained layer under the oxide scale. Hence, a nano-grained metal matrix layer can be consistently observed underneath the oxide scale during the entire experimental period (Fig. 11b). The high grain boundary density in the nano-grained layer will, in return, accelerate the outward diffusion of Cr and enhance the consumption of Cr in the

near-surface metal matrix.

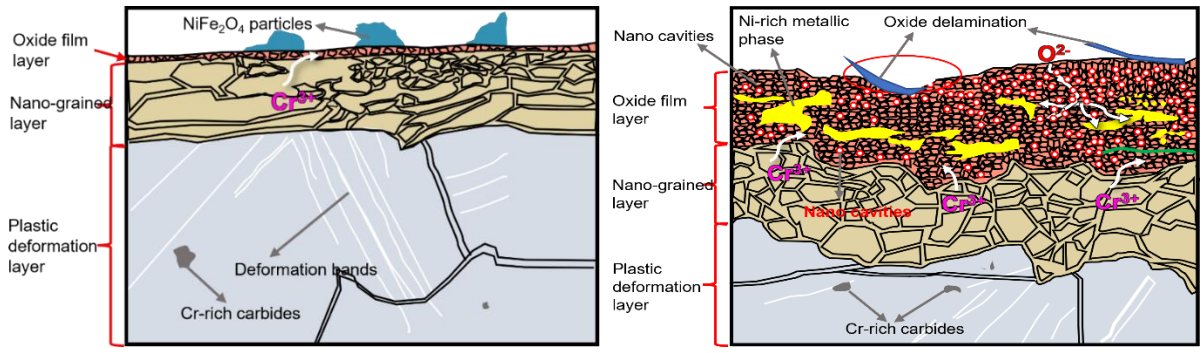


(a) (b)

Fig. 11. Schematic images showing the cross-sectional morphologies of A690 a) without and b) with fretting wear in the simulated PWR secondary water.

## 5. Conclusions

Cross-sections of the corrosion-resistant Ni-based A690 have been comprehensively studied by multiple advanced characterization techniques after fretting corrosion testing in simulated PWR secondary water. The major findings in this study can be summarized as follows:

1) A690 follows external oxidation when the surface is free of fretting wear, while localized internal oxidation is also observed due to the prior manufacturing-induced ununiform deformation in the near-surface matrix.

2) The relatively thick oxide scale on the worn scars is formed by the accelerated internal oxidation of A690 instead of the pile-up of oxide debris due to the different chemical composition distribution in comparison with the oxide scale formed by the pile-up of oxide debris.

3) The fretting wear introduces dynamic stress/strain between the contacting surface, which constantly break the integrity of the oxide scale, as well as resulting in the formation of a nano-grained matrix layer under the oxide scale. Although the nano-grained matrix layer usually could accelerate the Cr outward diffusion and result in a better corrosion resistance, the constant breakdown of the oxide scale integrity by the fretting wear would not enhance its corrosion resistance but accelerate the Cr consumption in the nano-grained matrix layer.

4) The fretting wear deteriorates the corrosion resistance of A690 mainly in three ways: a) reducing the thickness of the oxide scale; b) introducing nanocavities and nano-cracks into the grain boundaries of the oxide scale; c) accelerating Cr consumption in the near-surface nano-grained matrix.

## Acknowledgements

Shanghai Pujiang Program (21PJ1406400) is acknowledged for funding this research. Microstructural Characterization of Instrumental Analysis Center of SJTU is also gratefully acknowledged. The authors from University of Oxford would like to thank the EPSRC (EP/K040375/1, EP/N010868/1 and EP/R009392/1) grants for funding this research.

## References

[1] I.L. Pioro, R.B. Duffey, P.L. Kirillov, R. Panchal. Introduction: a survey of the status of electricity generation in the world. In Handbook of generation IV nuclear reactors (pp. 1-34). Woodhead Publishing, 2016.

[2] Z.B. Cai, Z.Y. Li, M.G. Yin, M.H. Zhu, Z.R. Zhou. A review of fretting study on nuclear power equipment. Tribology International, 144(2020) 106095.

[3] M.P. Kissane, A review of radionuclide behaviour in the primary system of a very-high-temperature reactor, Nucl. Eng. Des., 239 (2009) 3076-3091.

[4] R.L. Klueh, A.T. Nelson, Ferritic/martensitic steels for next-generation reactors, J. Nucl. Mater., 371 (2007) 37-52.

[5] S. Glasstone, A. Sesonske, Nuclear reactor engineering: reactor systems engineering, Springer Science & Business Media (2012).

[6] Z. Shen, L. Zhang, R. Tang, Q. Zhang. The effect of temperature on the SSRT behavior of austenitic stainless steels in SCW. Journal of Nuclear Materials, 454(2014) 274-282.

[7] Z. Shen, K. Chen, X. Guo, L. Zhang, 2019. A study on the corrosion and stress corrosion cracking susceptibility of 310-ODS steel in supercritical water. Journal of Nuclear Materials, 514, pp.56-65.

[8] T. Moss, W. Kuang, G.S. Was. Stress corrosion crack initiation in Alloy 690 in high temperature water. Current Opinion in Solid State and Materials Science, 22(2018) 16-25.

[9] X. Guo, P. Lai, L. Li, L. Tang, L. Zhang. Progress in studying the fretting wear/corrosion of nuclear steam generator tubes. Annals of Nuclear Energy, 144(2020) 107556.

[10] Z. Shen, K. Arioka, S. Lozano-Perez. A mechanistic study of SCC in Alloy 600 through high-resolution characterization. Corrosion Science, 132(2018) 244-259.

[11] Z. Shen, E. Roberts, N. Saravanan, P. Karamched, T. Terachi, T. Yamada, S. Wu, E. Tarleton, D.E.J. Armstrong, P.J. Withers, K. Arioka, S. Lozano-Perez, On the role of intergranular nanocavities in long-term stress corrosion cracking of Alloy 690, Acta Materialia, In Press, 2021.

[12] K. Arioka, R.W. Staehle, T. Yamada, T. Miyamoto, T. Terachi. Degradation of Alloy 690 after relatively short times. Corrosion, 72(2016) 1252-1268.

[13] W. Kuang, M. Song, G.S. Was. Insights into the stress corrosion cracking of solution annealed alloy 690 in simulated pressurized water reactor primary water under dynamic straining. Acta Materialia, 151(2018) 321-333.

[14] B.L. Dow. Steam generator progress report: revision 12. EPRI TR-106365, 1996.

[15] S.S. Hwang, C. Namgung, M.K. Jung, H.P. Kim, J.S. Kim, Rupture pressure of wear degraded Alloy 600 steam generator tubings, J. Nucl. Mater., 373 (2008), pp. 71-74.

[16] Root Cause Analysis Report for tube wear identified in the Unit 2 and Unit 3 Steam Generators of San Onofre Nuclear Generating Station, UES-20120254.

[17] P. Lai, X. Guo, L. Tang, X. Guo, L. Zhang. Effect of temperature on fretting wear behavior and mechanism of alloy 690 in water. Nuclear Engineering and Design, 327(2018) 51-60.

[18] J. Li, Y.H. Lu, Effects of displacement amplitude on fretting wear behaviors and mechanism of Inconel 600 alloy, Wear, 304 (2013), pp. 223-230.

[19] L. Xin, Z.H. Wang, J. Li, Y.H. Lu, T. Shoji. Fretting wear behavior and mechanism of Inconel 690 alloy related to the displacement amplitude. Tribology Transactions, 60(2017) 913-922.

[20] S.R. Soria, A. Tolley, A. Yawny, A study of debris and wear damage resulting from fretting of Incoloy 800 steam generator tubes against AISI Type 304 stainless steel, Wear, 368 (2016) 219-229.

[21] J.Y. Yun, M.C. Park, G.S. Shin, J.H. Heo, D.I. Kim, S.J. Kim. Effects of amplitude and frequency on the wear mode change of Inconel 690 SG tube mated with SUS 409. Wear, 313(2014) 83-88.

[22] J. Li, M. Ma, Y.H. Lu, L. Xin. Evolution of wear damage in Inconel 600 alloy due to fretting against type 304 stainless steel. Wear, 346(2016) 15-21.

[23] L. Xin, Y.H. Lu, T. Shoji, The role of material transfer in fretting wear behavior and mechanism of Alloy 690TT mated with Type 304 stainless steel, Mater Char, 130 (2017), pp. 250-259.

[24] J. Li, B.B. Yang, Y.H. Lu, L. Xin, Z.H. Wang, T. Shoji. The degradation mechanism of Inconel 690TT induced by fretting wear in air. Tribology International, 116(2017) 147-154.

[25] S.A. Soria, A. Tolley, A. Yawny, Characterization of damage and triboparticles resulting from fretting of incoloy 800 steam generator tubes against different materials, Wear, 390 (2017), pp. 198-208.

[26] L. Xin, B.B. Yang, Z.H. Wang, J. Li, Y.H. Lu, T. Shoji. Microstructural evolution of subsurface on Inconel 690TT alloy subjected to fretting wear at elevated temperature. Materials & Design, 104(2016) 152-161.

[27] L. Xin, B.B. Yang, J. Li, Y.H. Lu, T. Shoji. Wear damage of Alloy 690TT in partial and gross slip fretting regimes at high temperature. Wear, 390(2017) 71-79.

[28] X. Mi, Z.B. Cai, X.M. Xiong, H. Qian, L.C. Tang, Y.C. Xie, J.F. Peng, M.H. Zhu. Investigation on fretting wear behavior of 690 alloy in water under various temperatures. Tribology International, 100(2016) 400-409.

[29] X.Y. Zhang, J.H. Liu, Z.B. Cai, J.F. Peng, M.H. Zhu, P.D. Ren. Experimental study of the fretting wear behavior of Incoloy 800 alloy at high temperature. Tribology Transactions, 60(2017) 1110-1119.

[30] D.K. Park, S.W. Woo, D.H. Yoon, I. Chung. A study on fretting fatigue life for the Inconel alloy 600 at high temperature. Nuclear engineering and design, 240(2010) 2521-2527.

[31] L. Xin, M. Ma, Y. Lu, T. Shoji. Comparative study on fretting wear behaviors of Alloy 600MA in dry air and deionized water conditions. Wear, 418(2019) 167-179.

[32] J. Li, B.B. Yang, Y.H. Lu, L. Xin, Z.H. Wang, T. Shoji. The effects of electrochemical polarization condition and applied potential on tribocorrosion behaviors of Inconel 690 alloys in water environment. Materials & Design, 119(2017) 93-103.

[33] L. Xin, Y. Han, L. Ling, Y. Lu, T. Shoji. Surface Oxidation and Subsurface Microstructure Evolution of Alloy 690TT Induced by Partial Slip Fretting Corrosion in High-Temperature Pure Water. Acta Metallurgica Sinica (English Letters), 34(2021) 543-554.

[34] L. Xin, Y. Han, L. Ling, Y. Lu, T. Shoji. Effects of dissolved oxygen on partial slip fretting corrosion of Alloy 690TT in high temperature pure water. Journal of Nuclear Materials, 542(2020) 152483.

[35] X. Guo, P. Lai, L. Tang, J. Lu, J. Wang, L. Zhang. Fretting wear of alloy 690 tube mated with different materials in high temperature water. Wear, 400(2018) 119-126.

[36] X. Guo, P. Lai, L. Tang, K. Chen, L. Zhang. Time-dependent wear behavior of alloy 690 tubes fretted against 405 stainless steel in high-temperature argon and water. Wear, 414(2018) 194-201.

[37] X. Guo, P. Lai, L. Tang, J. Wang, L. Zhang. Effects of sliding amplitude and normal load on the fretting wear behavior of alloy 690 tube exposed to high temperature water. Tribology International, 116(2017) 155-163.

[38] H. Ming, X. Liu, Z. Zhang, J. Wang, E.H. Han. Effect of normal force on the fretting wear behavior of Inconel 690 TT against 304 stainless steel in simulated secondary water of pressurized water reactor. Tribology International, 126(2018) 133-143.

[39] J. Liao, X. Wu, J. Tan, L. Tang, H. Qian, Y. Xie. Fretting corrosion fatigue of Alloy 690 in high-temperature pure water. Corrosion Science, 133(2018) 423-431.

[40] L. Xin, B.B. Yang, Z.H. Wang, J. Li, Y.H. Lu, T. Shoji. Effect of normal force on fretting wear behavior and mechanism of Alloy 690TT in high temperature water. Wear, 368(2016) 210-218.

[41] L. Xin, Y.H. Lu, Y. Otsuka, Y. Mutoh, Z.H. Wang, T. Shoji. The role of frequency on fretting corrosion of Alloy 690TT against 304 stainless steel in high temperature high pressure water. Materials Characterization, 134(2017) 260-273.

[42] L. Luo, M. Su, P. Yan, L. Zou, D.K. Schreiber, D.R. Baer, Z. Zhu, G. Zhou, Y. Wang, S.M. Bruemmer, Z. Xu. Atomic origins of water-vapour-promoted alloy oxidation. Nature materials, 17(2018) 514-518.

[43] D.G. Xie, Z.J. Wang, J. Sun, J. Li, E. Ma, Z.W. Shan. In situ study of the initiation of hydrogen bubbles at the aluminium metal/oxide interface. Nature materials, 14(2015) 899-903.

[44] A. King, G. Johnson, D. Engelberg, W. Ludwig, J. Marrow. Observations of intergranular stress corrosion cracking in a grain-mapped polycrystal. Science, 321(2008) 382-385.

[45] Z. Shen, D. Tweddle, H. Yu, G. He, A. Varambhia, P. Karamched, F. Hofmann, A.J. Wilkinson, M.P. Moody, L. Zhang, S. Lozano-Perez. Microstructural understanding of the oxidation of an austenitic stainless steel in high-temperature steam through advanced characterization. Acta Materialia, 194(2020) 321-336.

[46] Z. Shen, K. Chen, H. Yu, B. Jenkins, Y. Ren, N. Saravanan, G. He, X. Luo, P. Bagot, M.P. Moody, L. Zhang. New insights into the oxidation mechanisms of a ferritic-martensitic steel in high-temperature steam. Acta Materialia, 194(2020) 522-539.

[47] K. Chen, L. Zhang, S. Wu, Z. Shen. High-resolution characterization of the internal and external oxidation of austenitic alloys in supercritical water. Scripta Materialia, 197(2021) 113814.

[48] J.Y. Yun, M.C. Park, G.S. Shin, J.H. Heo, D.I. Kim, S.J. Kim. Effects of amplitude and frequency on the wear mode change of Inconel 690 SG tube mated with SUS 409. Wear, 313(2014) 83-88.

[49] J. Jiang, F.H. Stott, M.M. Stack. Some frictional features associated with the sliding wear of the nickel-base alloy N80A at temperatures to 250°C. Wear, 176 (1994) 185-194.

[50] Xiangzhen Xue, Sanmin Wang, Bo Li. Modification methodology of fretting wear in involute spline. Wear, 368–369 (2016) 435-444.

[51] Arnab Ghosh, Ben Leonard, Farshid Sadeghi. A stress based damage mechanics model to simulate fretting wear of Hertzian line contact in partial slip. Wear, 307 (2013) 87-99.

[52] F. Huang, J. Wang, E.H. Han, W. Ke. Microstructural characteristics of the oxide films formed on Alloy 690 TT in pure and primary water at 325 C. Corrosion Science, 76(2013) 52-59.

[53] W. Kuang, X. Wu, E.H. Han, J. Rao. The mechanism of oxide film formation on Alloy 690 in oxygenated high temperature water. Corrosion science, 53(2011) 3853-3860.

[54] I. Betova, M. Bojinov, V. Karastoyanov, P. Kinnunen, T. Saario. Effect of water chemistry on the oxide film on Alloy 690 during simulated hot functional testing of a pressurised water reactor. Corrosion Science, 58(2012) 20-32.

[55] Z. Shen, D. Tweddle, M. T. Lapington, B. Jenkins, D. Du, L. Zhang, M.P. Moody, S. Lozano-Perez. Observation of internal oxidation in a 20% cold-worked Fe-17Cr-12Ni stainless steel through high-resolution characterization. Scripta Materialia, 173(2019) 144-148.

[56] K. Chen, Z. Shen. A study on the surface and crack tip oxidation of alloy 600 through high-resolution characterization. Corrosion Science, 169(2020) 108616.

[57] Z. Shen, K. Chen, D. Tweddle, G. He, K. Arioka, S. Lozano-Perez. Characterization of the crack initiation and propagation in Alloy 600 with a cold-worked surface. Corrosion Science, 152(2019) 82-92.

[58] Y.L. Han, J.N. Mei, Q.J. Peng, E.H. Han, W. Ke. Effect of electropolishing on corrosion of Alloy 600 in high temperature water. Corros. Sci., 98 (2015) 72-80.

[59] S. Lozano-Perez, K. Kruska, I. Iyengar, T. Terachi, T. Yamada. The role of cold work and applied stress on surface oxidation of 304 stainless steel. Corrosion Science, 56(2012) 78-85.

[60] D. Jullian, A. Prillieux, J. Zhang, D.J. Young. Oxygen permeability of Fe-Ni-Cr alloys at 1100 and 1150° C under carbon-free and carbon-containing gases. Materials and Corrosion, 68(2017) 197-204.

[61] L.S. Darken. Some Observation on Atoms and Imperfection. Transactions of the ASM. 54(1961) 600-642.

[62] E.P. Song, B. Hwang, S. Lee, N.J. Kim, J. Ahn. Correlation of microstructure with hardness and wear resistance of stainless steel blend coatings fabricated by atmospheric plasma spraying, Mater. Sci. Eng.: A, 429 (2006) 189-195.

[63] J. Hardell, S. Hernandez, S. Mozgovoy, L. Pelcastre, C. Courbon, B. Prakash. Effect of oxide layers and near surface transformations on friction and wear during tool steel and boron steel interaction at high temperatures, Wear, 330–331 (2015) 223-229.

[64] J.C. Haygarth, L.J. Fenwick. Improved wear resistance of zirconium by enhanced oxide films, Thin Solid Films, 118 (1984) 351-362.

[65] M. Yasir, C. Zhang, W. Wang, P. Xu, L. Liu. Wear behaviors of Fe-based amorphous composite coatings reinforced by Al2O3 particles in air and in NaCl solution, Mater. Des., 88 (2015) 207-213.

[66] J. Y. Yun, H. S. Lee, D. H. Hur, W. S. Kang, C. H. Bae, S. J. Kim. Effect of oxidation film on the fretting wear behavior of Alloy 690 steam generator tube mated with SUS 409. Wear, 368(2016) 344-349.